applied sciences

MDPI

Article

A Novel, Soft, Cable-Driven Parallel Robot for Minimally Invasive Surgeries Based on Folded Pouch Actuators

Jianlin Yang [1,2,†], Xinxin Li [2,†], Mark Runciman [2], James Avery [2], Zhangxi Zhou [2], Zhijun Sun [1] and George Mylonas [2,*]

[1] State Key Laboratory of Mechanics and Control of Aerospace Structures, Nanjing University of Aeronautics and Astronautics, Nanjing 210016, China
[2] The Hamlyn Centre, Institute of Global Health Innovation, Imperial College London, London W2 1PF, UK
* Correspondence: george.mylonas@imperial.ac.uk
† These authors contributed equally to this work.

Abstract: This paper introduces a soft, cable-driven parallel robot for minimally invasive surgeries. The robot comprises a pneumatic inflatable scaffold, six hydraulic, folded pouch actuators, and a hollow, cylindrical end-effector offering five degrees of freedom. A key development is the design of the pouch actuators, which are small, low-profile, simple structures, capable of a high stroke of 180° angular displacement. The scaffold, actuators, and plastic cables are economically and rapidly fabricated using laser cutting and welding techniques. Constructed primarily from soft plastic materials, the robot can be compactly folded into a cylinder measuring 110 mm in length and 14 mm in diameter. Upon inflation, the scaffold transforms into a hexagonal prism structure with side lengths of 34 mm and edge lengths of 100 mm. The kinematic model of the robot has been developed for workspace calculation and control purposes. A series of tests have been conducted to evaluate the performance of the actuator and the robot. Repeatability tests demonstrate the robot's high repeatability, with mean and root mean square errors of 0.3645 mm and 0.4186 mm, respectively. The direct connection between the end-effector and the actuators theoretically eliminates cable friction, resulting in a hysteresis angle of less than 2°, as confirmed by the tracking results. In addition, simulated surgical tasks have been performed to further demonstrate the robot's performance.

Keywords: minimally invasive surgery; soft actuator; soft robot; cable-driven parallel robot

Citation: Yang, J.; Li, X.; Runciman, M.; Avery, J.; Zhou, Z.; Sun, Z.; Mylonas, G. A Novel, Soft, Cable-Driven Parallel Robot for Minimally Invasive Surgeries Based on Folded Pouch Actuators. *Appl. Sci.* **2024**, *14*, 4095. https://doi.org/10.3390/app14104095

Academic Editors: Carlos J. Pérez Del Pulgar and Irene Rivas Blanco

Received: 15 March 2024
Revised: 8 May 2024
Accepted: 9 May 2024
Published: 11 May 2024

1. Introduction

Existing flexible endoscopic systems provide limited instrument dexterity. This hinders the uptake of emerging superior techniques, like endoscopic submucosal dissection (ESD), which have shown superior *en bloc* resection rates for early gastrointestinal cancers compared to conventional methods [1]. Utilizing flexible gastrointestinal endoscopes, diverse robotic platforms have been developed and assessed in both preclinical and clinical scenarios to validate their effectiveness and safety [2]. Most of these platforms can perform ESD. However, they predominantly utilize cable-driven articulated manipulators, which face common limitations in terms of their flexibility, force transmission, and precision, which can be significant due to the long and tortuous human colon.

Soft robots, known for their ability to conform to environments, hold significant promise for applications in minimally invasive surgeries (MISs) [3]. They are anticipated to address challenges faced by conventional rigid robots, offering innovative solutions for clinical interventions and surgical procedures. Particularly in delicate surgical scenarios like endoluminal and transluminal surgeries, where adaptation to the patient's anatomical structure is crucial, soft robots exhibit great potential. However, the inherent softness of these robots also presents substantial challenges, including a low force exertion, limited controllability, and a lack of sensing capabilities [4].

Parallel robots employ multiple kinematic chains to connect the moving platform with the base platform [5], while they offer advantages such as having high speeds, stiffnesses, and payload capacities. Many parallel robots have been developed for MISs [6–9]. Khalifa et al. introduced a dexterous endoscopic parallel manipulator for MISs with three limbs featuring identical kinematic structures and three degrees of freedom (DOFs) [6]. Liu et al. proposed a dual-arm single-port-access surgical robot incorporating a visual module and two surgical manipulators [7]. Each manipulator, with six DOFs, consists of two parallel mechanisms connected in series, expanding the end-effector's workspace while maintaining high stiffness. Li et al. presented a flexible robotic system with variable stiffness for transoral robotic surgeries, achieving compliant movements through flexible three-prismatic-universal parallel mechanisms using nickel–titanium rods [8]. Andrew et al. developed a surgical parallel/continuum manipulator with a standard Stewart–Gough arrangement, combining the precision and power of rigid-link parallel robots with the simplicity, compactness, and compliance of continuum robots [9]. However, these robots face limitations when required to navigate through narrow and confined surgical spaces, such as the colon, due to their rigidity. Even the robots driven by flexible rods are still relatively rigid.

Cable-driven parallel robots (CDPRs) replace the rigid kinematic chains of parallel mechanisms with cables, offering advantages such as high payload capacities, dynamic capabilities, and large workspaces [10]. The CYCLOPS concept, introduced by Mylonas et al., employs the CDPR structure to create a versatile endoscopic surgical robot with bimanual dexterity [11]. Driven by flexible Bowden cable mechanisms, the CYCLOPS robot can be introduced into the colon using an endoscope. In subsequent developments, a fully soft CDPR robot was created boasting an inflatable scaffold made of low-profile and low-cost plastic materials [12]. However, the robot still utilized long Bowden cables, resulting in issues of hysteresis and reduced accuracy due to the difficulty in modeling the effects of cables bending over long distances. To address this challenge, Runciman et al. proposed an open-loop, controlled, soft, inflatable robot driven by contraction-based hydraulic pouch actuators [13]. While this approach eliminates the friction associated with Bowden cable mechanisms using hydraulic transmission, three short cables connecting the actuators to the effector through PTFE tubes still suffer from friction and hysteresis. Additionally, a pulley for displacement amplification was required due to the limited stroke of the pouch actuator.

Pouch actuators, as seen in Figure 1a and initially introduced in [14], are characterized by their low profile, low cost, and having nearly zero volume when deflated, making them highly suitable for applications in confined spaces. However, their theoretical contraction ratio is limited to 36.3% of their unactuated length. Various approaches have been explored to enhance the contraction ratio of pouch actuators [15–19]. These approaches include internal and external constraints [15], rigid amplification mechanisms [16], series–parallel hybrid arrangements [17], the addition of gussets [18], and stacked pouches pushing outer structures [19]. These methods can improve contraction ratios, but their structures and manufacturing processes are relatively complex.

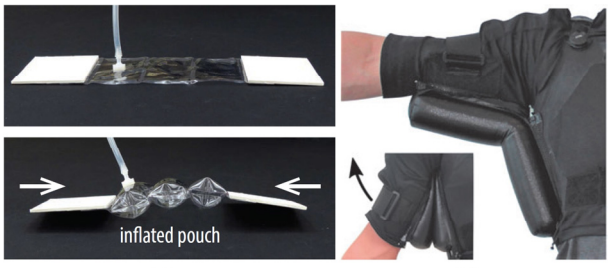

Figure 1. A pouch actuator. (**a**) A contraction-based pouch actuator [14]. (**b**) A folded pouch actuator [20].

In contrast, folded actuators (shown in Figure 1b, as an example), constructed from an airbag, can achieve large angular displacements and generate considerable force outputs [20–23]. They exhibit flexibility, adaptability, simplicity, low profiles, and low costs. When deflated, their volume is minimal, yet they can achieve significant expansion upon inflation. So far, they have been used predominantly with soft wearable devices to assist joint movement. More recently, artificial muscles based on folded pouch actuators achieved impressive contraction ratios (up to 92.9%) [24–26]. Moreover, robotic elbows, jumping robots, and soft grippers have been developed based on folded pouch actuators [25,26].

This paper introduces a novel soft CDPR based on folded hydraulic pouch actuators designed for MISs, specifically colorectal surgeries, as an improvement over a range of existing CDPR mechanisms. The proposed design allows the end-effector to be directly connected to the actuators, resulting in there being no friction or hysteresis, which are issues typically associated with the use of Bowden cables in previous CDPR-based robots [12,13]. The robot is a monolithic device crafted entirely from low-cost, flexible plastic film laminates, enabling the robot to be single use, which has certain advantages in MISs when compared with reusable devices that require sterilization before each use.

2. Robot System Components and Fabrication

2.1. Design Considerations

The most important design considerations are the robot size, operational workspace, and force exertion. The human colon's diameter is in the range of 30 to 80 mm, with a widely accepted average of 45 mm [27], and is reasonably distensible. Therefore, the robot must be sufficiently close to the lower limit for comfortable introduction, while not exceeding the colon's average diameter upon deployment at the surgical site. Colorectal tumor sizes typically range from 6.2 to 43.6 mm [28], determining the desirable operational workspace of the robot, if its repositioning within the colon is not desirable. Ranzani et al. [29] measured forces of 0.9 N and 0.58 N, respectively, for lifting and pulling mucosa in the rectum during transanal endoscopic surgeries. This is a valuable design reference for the robot's force exertion capabilities.

2.2. Folded Pouch Actuator

In Figure 2, a folded pouch actuator is depicted as an initially deflated, folded, flat chamber with two cables connected to its ends. Upon inflation, the actuator deploys and lifts a weight. The weight reaches its highest position when the pouch actuator is fully deployed. Figure 2(d1–d3) shows an actuator prototype made of plastic film and fabricated using a laser welding device developed in [12]. The cables connected to the chamber are also made of plastic film, allowing them to be fabricated together with the actuator. The actuator can be pneumatic or hydraulic, and it achieves a large stroke through folding and unfolding, capable of serving as a large-stroke artificial muscle.

2.3. Planar CDPRs Driven by Folded Actuators

A single folded pouch actuator can only provide one DOF. However, by combining multiple of these actuators, additional DOFs can be achieved. In Figure 3a, a diagram of a 2-DOF planar CDPR is presented. The robot comprises two folded actuators, each connected to one cable. Each actuator functions as a link structure. By utilizing the force of gravity, the robot offers two DOFs, allowing for the movement of the weight in upward, downward, leftward, and rightward directions, as illustrated in Figure 3(d1–d4).

As shown in Figure 3b, if the two cables are connected to a rod-shaped effector instead of a point, the planar robot exhibits three DOFs, but it is underconstrained. This implies that the position and orientation cannot be controlled independently. By increasing the number of pouch actuators and cables to four, the planar CDPR can achieve full constraint, as shown in Figure 3c. In this configuration, both the planar position and the orientation can be controlled independently, enabling the effector to move forward, backward, move left, move right, turn left, and turn right, as seen in Figure 4 (Supplementary Materials).

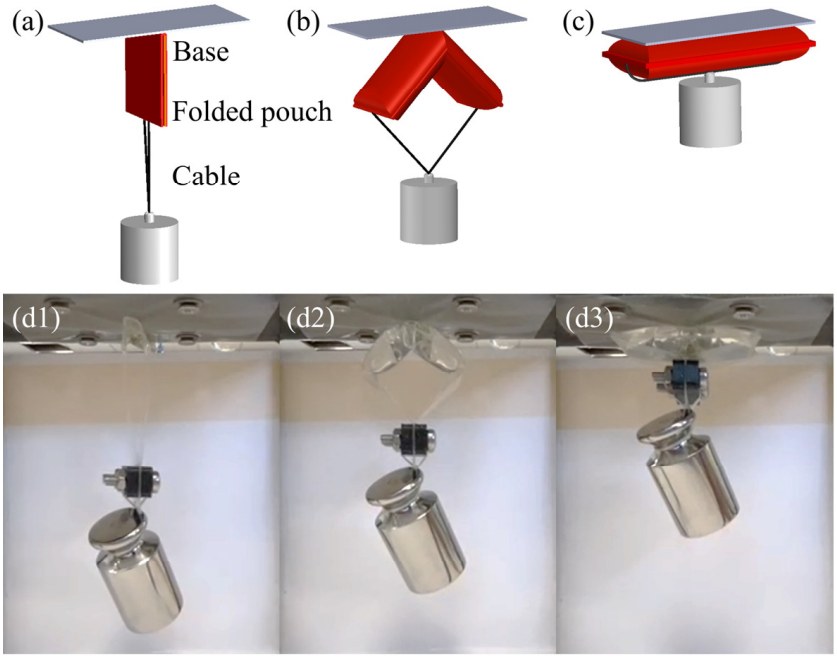

Figure 2. A folded pouch actuator. (**a**–**c**) A 3D diagram and a working principle of an actuator. (**d1**–**d3**) A prototype of the folded pouch actuator. The folded actuator deployed to lift a weight of 100 g.

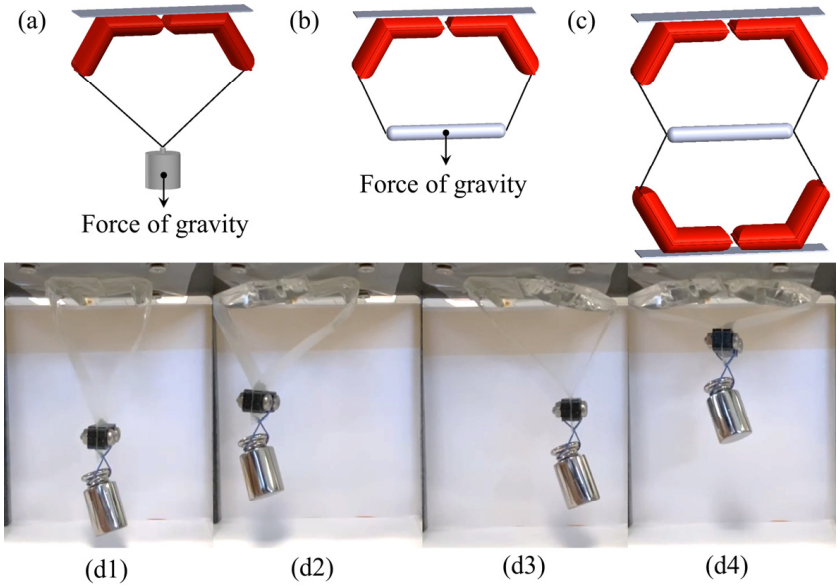

Figure 3. The concepts of three planar CDPRs. (**a**) A 2-DOF CDPR with a mass point effector. (**b**) An underconstrained 3-DOF robot with a rod-shaped effector. (**c**) A completely constrained 3-DOF robot. (**d1**–**d4**) A prototype of the 2-DOF CDPR. The effector was at the (**d1**) lowest, (**d2**) leftmost, (**d3**) rightmost, and (**d4**) highest position.

2.4. The Design of the Robot for MISs

By converting the robot from a 2D to a 3D configuration and by increasing the number of pouch actuators to six, five DOFs can be implemented (three translational, and yaw and pitch). In previous 5-DOF CDPR robots [11,12], we have demonstrated the feasibility of performing ESD. Figure 5 shows the 3D model of the robot, comprising a hexagonal prismatic inflatable scaffold, six folded pouch actuators, and an over-tube effector. There exists no friction or hysteresis, theoretically, as the end-effector is directly connected to

the actuators without using any Bowden cable mechanisms. The actuators are hydraulic, circumventing the friction associated with Bowden cables, commonly used in surgical tools, and allow for open-loop control due to the incompressibility of liquids. Six folded actuators are positioned between the beam units of the scaffold, and six cables are connected to the over-tube. To ensure the validity of the established kinematics, a robust scaffold is essential. In this design, two inflatable triangular support structures are mounted on the top and bottom of the prismatic scaffold to enhance the scaffold's stiffness. The planar robot configuration in Figure 3c is discarded as the scaffold deformation will be larger if the fixed parts of the actuators are mounted in the middle of scaffold beam units.

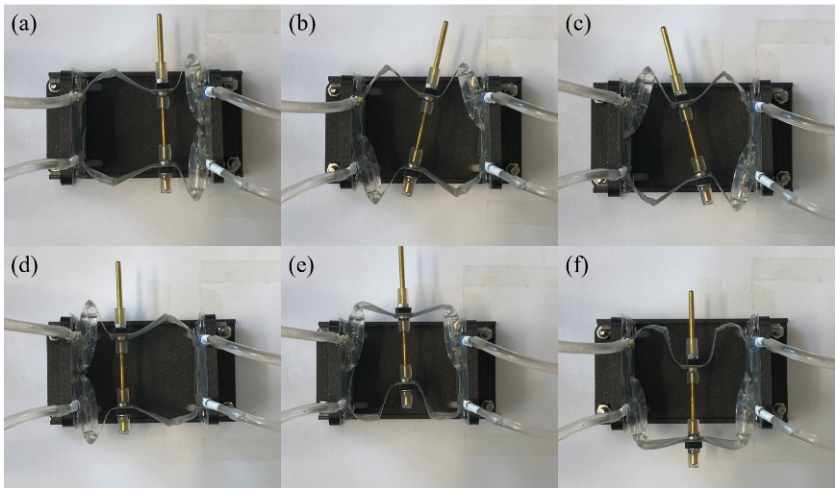

Figure 4. A prototype of the 3-DOF completely constrained CDPR. The effector was driven to (**a**) translate right, (**b**) turn right, (**c**) turn left, (**d**) translate left, (**e**) translate forward, and (**f**) translate backward.

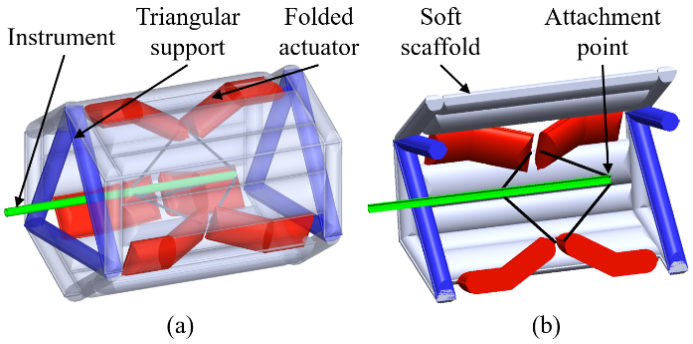

Figure 5. A 3D model of the inflatable CDPR. (**a**) A side view and (**b**) cross-section view of the robot.

2.5. Robot Kinematics

Figure 6 shows the simplified diagram used for the inverse kinematic analysis of the robot. The actuator is treated as a rigid robotic arm. Symbols are defined as follows: a right subscript i indicates the arm or the cable number, and a left superscript denotes the coordinate system where the value is defined. Σ_0 is the base coordinate system, Σ_p is the local coordinate system attached on the tip of the over-tube, Σ_{m_i} is the coordinate system fixed at the rotation center of an arm (the arm coordinate system), $\boldsymbol{r}_i$ is the position of the cable attachment point on the end-effector in the local coordinate system, $\mathbf{s}_i$ is a vector along the rotating part of the arm, $\boldsymbol{l}_i$ is a vector along a cable, $\boldsymbol{h}_i$ is a vector from the rotation center of an arm to the cable attachment point at the end-effector, $\boldsymbol{u}_i$ is a unit vector along a cable, $\boldsymbol{A}_i$ is the position of the center of rotation of an arm, $\boldsymbol{F}_i$ is the position of the connecting point between the arm and the cable, ϕ_{m_i} is the angle between the rotating arm and the x-axis of the arm coordinate system, l_{c_i} is the cable length, and l_a is the rotating arm length.

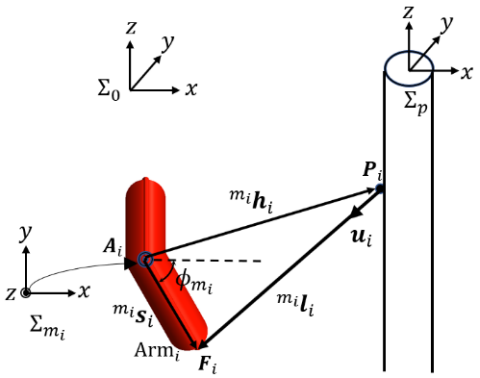

Figure 6. The nomenclature and coordinates of the robot.

The position of the attachment point between the cable and end-effector is

$$\boldsymbol{P}_i = \boldsymbol{P} + {}^0\boldsymbol{R}_p \boldsymbol{r}_i \tag{1}$$

where $\boldsymbol{P}$ is the end-effector tip position in the base coordinate system, and ${}^0\boldsymbol{R}_p$ denotes the orientation matrix from the local coordinate system to the base coordinate system. Due to there being only yaw and pitch rotations for the end-effector, the rotation matrix is ${}^0\boldsymbol{R}_p = \boldsymbol{R}_y(\beta)\boldsymbol{R}_x(\gamma)$, where β and γ are Euler angles.

A vector along a cable in the arm coordinate system is defined as

$${}^{m_i}\boldsymbol{l}_i = {}^{m_i}\boldsymbol{s}_i - {}^{m_i}\boldsymbol{h}_i \tag{2}$$

where ${}^{m_i}\boldsymbol{h}_i$ can be expressed by using the orientation matrix ${}^{m_i}\boldsymbol{R}_0$ from the base coordinate system to the arm coordinate system:

$${}^{m_i}\boldsymbol{h}_i = {}^{m_i}\boldsymbol{R}_0(\boldsymbol{P}_i - \boldsymbol{A}_i) \tag{3}$$

The cable length l_{c_i} is constant:

$$\begin{aligned} {l_{c_i}}^2 &= \|{}^{m_i}\boldsymbol{l_i}\|^2 \\ &= {}^{m_i}{l_{x_i}}^2 + {}^{m_i}{l_{y_i}}^2 + {}^{m_i}{l_{z_i}}^2 \\ &= (l_a \cos\phi_{m_i} - {}^{m_i}h_{x_i})^2 + (l_a \sin\phi_{m_i} - {}^{m_i}h_{y_i})^2 + (-{}^{m_i}h_{z_i})^2 \end{aligned} \tag{4}$$

Substitute $\cos\alpha = \frac{{}^{m_i}h_{x_i}}{\sqrt{{}^{m_i}{h_{x_i}}^2 + {}^{m_i}{h_{y_i}}^2}}$ and $\sin\alpha = \frac{{}^{m_i}h_{y_i}}{\sqrt{{}^{m_i}{h_{x_i}}^2 + {}^{m_i}{h_{y_i}}^2}}$ into Equation (4):

$$\cos(\alpha - \phi_{m_i}) = \frac{{l_a}^2 + \|{}^{m_i}\boldsymbol{h}_i\|^2 - {l_{c_i}}^2}{2l_a\sqrt{{}^{m_i}{h_{x_i}}^2 + {}^{m_i}{h_{y_i}}^2}} \tag{5}$$

There exist two solutions for the inverse kinematics problem:

$$\phi_{m_i}(1) = \tan^{-1}\frac{{}^{m_i}h_{y_i}}{{}^{m_i}h_{x_i}} - \cos^{-1}\frac{{l_a}^2 + \|{}^{m_i}\boldsymbol{h}_i\|^2 - {l_{c_i}}^2}{2l_a\sqrt{{}^{m_i}{h_{x_i}}^2 + {}^{m_i}{h_{y_i}}^2}} \tag{6}$$

$$\phi_{m_i}(2) = \tan^{-1}\frac{{}^{\mathrm{m_i}}\mathrm{h_{y_i}}}{{}^{m_i}h_{x_i}} + \cos^{-1}\frac{{l_a}^2 + \|{}^{m_i}\boldsymbol{h}_i\|^2 - {l_{c_i}}^2}{2l_a\sqrt{{}^{m_i}{h_{x_i}}^2 + {}^{m_i}{h_{y_i}}^2}} \tag{7}$$

However, one solution should be discarded as the folded actuator can only generate torque in one direction, and the correct solution should satisfy the following condition:

$$\left[{}^{m_i}\boldsymbol{h}_i^p \times {}^{m_i}\boldsymbol{s}_i\right]_z < 0 \tag{8}$$

where ${}^{m_i}\boldsymbol{h}_i^p$ is the projection vector of ${}^{m_i}\boldsymbol{h}_i$ in the x-y plane of the arm coordinate system Σ_{m_i}, and ${}^{m_i}\boldsymbol{s}_i = [l_a\cos\phi_{m_i}, l_a\sin\phi_{m_i}, 0]^T$. In this case, Equation (6) is the inverse kinematic solution and a condition should be satisfied: $\phi_{m_i} \in [-\pi/2, \pi/2]$. Another condition that should be satisfied is the force and torque equilibrium at the end-effector:

$$\boldsymbol{J}^T\boldsymbol{t} + \boldsymbol{f} = \boldsymbol{0} \tag{9}$$

where $\boldsymbol{t} = \{t_1, t_2, t_3, t_4, t_5, t_6\}^T$ is the cable tension vector, $\boldsymbol{f}$ denotes the external wrench, and the structure matrix depending on the pose of the effector is $\boldsymbol{J}^T$:

$$\boldsymbol{J}^T = \begin{bmatrix} \boldsymbol{u}_1 \cdots \boldsymbol{u}_6 \\ \boldsymbol{v}_1 \cdots \boldsymbol{v}_6 \end{bmatrix} \tag{10}$$

where the unit vector $\boldsymbol{u}_i = \boldsymbol{l}_i/\|\boldsymbol{l}_i\|$ and $\boldsymbol{v}_i = \boldsymbol{u}_i \times \boldsymbol{P}_i$. The pose of the end-effector should satisfy Equation (9) with $t_i > 0$, and $\phi_{m_i} \in [-\pi/2, \pi/2]$. The corresponding feasible solutions for vector $\boldsymbol{t}$ can be found in [30], and the procedure is as follows: (1) The external wrench $\boldsymbol{f}$ can usually be assumed to be $\boldsymbol{0}$. (2) An initial value greater than 0 can be assigned to the tension of one cable (e.g., t_1 = 1) to solve for the tension of all other cables according to Equation (9). If the tension values of other cables are all greater than 0, the current pose of the effector is considered to satisfy the force and torque equilibrium, and the position of the robot tip can be included in the robot's feasible workspace. The actuator bending angle ϕ_{a_i} can be calculated by

$$\phi_{a_i} = \frac{\pi}{2} - \phi_{m_i}(1) = \frac{\pi}{2} - \tan^{-1}\frac{{}^{m_i}h_{y_i}}{{}^{m_i}h_{x_i}} + \cos^{-1}\frac{{l_a}^2 + \|{}^{m_i}\boldsymbol{h}_i\|^2 - {l_{c_i}}^2}{2l_a\sqrt{{}^{m_i}h_{x_i}{}^2 + {}^{m_i}h_{y_i}{}^2}} \tag{11}$$

where ${}^{m_i}\boldsymbol{h}_i = {}^{m_i}\boldsymbol{R}_0\left(\boldsymbol{P} + {}^0\boldsymbol{R}_p\boldsymbol{r}_i - \boldsymbol{A}_i\right)$ according to Equations (1) and (3), and it includes the robot tip position $\boldsymbol{P}$ and the orientation matrix ${}^0\boldsymbol{R}_p$.

2.6. Robot Manufacturing

Using a laser welding manufacturing technique as shown in [12], the low-profile inflatable structures can be fabricated economically and rapidly. The used thermoplastic sheet is a biocompatible polyethylene (PE) polyethylene terephthalate (PET) solvent-bonded triple laminate PE/PET/PE, with a thickness of 30/60/30 µm. The layers for the scaffold and actuators were welded following the welding patterns in Figure 7. The welded plastic sheet for the actuators was laser-cut (FLUX BEAMO, Europe) along the cutting lines in Figure 7c to generate the plastic cables. After removing redundant material, the scaffold, triangular support, and actuators are shown in Figure 8a–c. As shown in Figure 8d,e, the actuators and triangular support were manually welded to the scaffold using a soldering iron at purple lines and blue points in Figure 7. Subsequently, edges were welded along the green lines. Finally, the end-effector and tubes for driving the actuators and pressurizing the scaffold were integrated, and Figure 8f shows the inflated robot prototype.

Figure 7 illustrates the dimensions of the robot components. The hexagonal prismatic scaffold has a side length of 34 mm, resulting in an equivalent diameter of 65 mm, which is larger than the colon's average diameter but still falls within the typical colon size range of 30 to 80 mm [27]. Also, the robot is scalable and the dimensions of its components can be easily adjusted to suit different clinical situations and requirements.

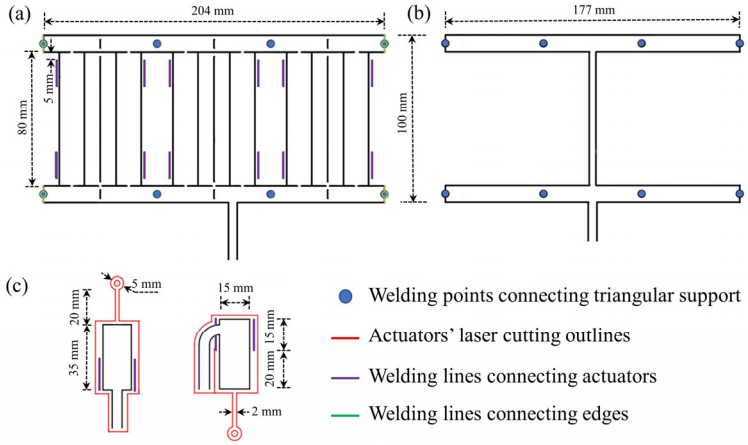

Figure 7. The welding and cutting patterns for producing (**a**) the scaffold, (**b**) the triangular support, and (**c**) the actuators.

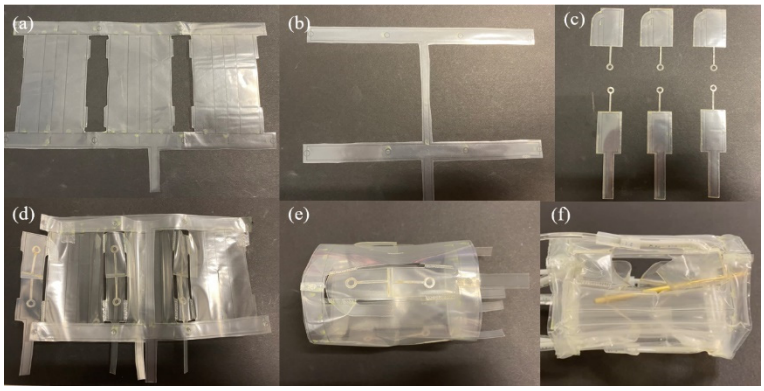

Figure 8. Robot fabrication. (**a**–**c**) The scaffold, triangular support, and actuator plastic film pieces were welded according to the patterns and cut either by a laser cutter or manually. (**d**) A photograph of how to manually weld the actuators and the triangular support onto the scaffold. (**e**) A photograph of how to manually weld edges to generate a hollow structure. (**f**) Lastly, the structure can be pressurized and formed into a hexagonal prism.

3. Methods and Results

3.1. Actuator Characteristics

Figure 9a shows the setup for testing the characteristics of the actuators. A 1 m-long tube with a 3 mm outer diameter connects the folded hydraulic actuator to a syringe pump. A pressure sensor (SparkFun MS5803-14BA) close to the syringe pump measures the pressure inside the actuator, with the sensor data recorded via an Arduino Uno microprocessor, which also controls the syringe pump. Figure 9b provides a detailed diagram of the actuator test platform. The folded actuator is fixed to both a fixed pad and a rotating pad which is rotated by the unfolding of the actuator. The cable, fixed onto and wound around a cylindrical rod connected to the rotating pad, is attached to a cart-like slider. A weight is used to pretension the cable. The pad rotation leads to the cable displacement, which is obtained by measuring the distance of two retro-reflective markers fixed on the bench and the slider, respectively. The positions of the two reflective markers were recorded by the OptiTrack (NaturalPoint, Corvallis, OR, USA) optical motion tracking system. The rotation angle of the rotating pad is calculated as the cable displacement divided by the radius of the cylindrical rod. An assumption made in the test is that the rotation angle of the actuator is equivalent to the pad rotation angle. Before testing, any air bubbles in the hydraulic lines were purged.

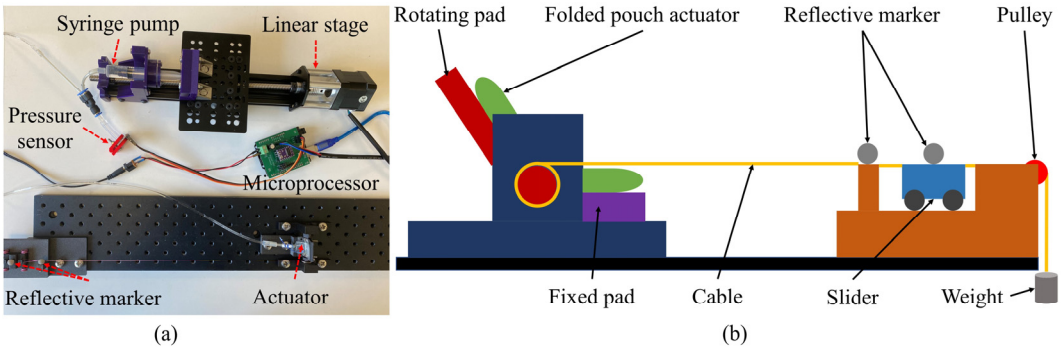

Figure 9. The test platform for the actuator characteristics. (**a**) The test setup. (**b**) A diagram of the actuator test platform.

The maximum water volume within the folded actuator is 2 mL, allowing the actuator to fully straighten. Based on the kinematics of the robot, the actuator's rotation angle is between 90° and 180° given the specified dimensions of each component in Figure 7. Therefore, testing was conducted within the rotation angle range of 90° to 180°. The water volume varies from 1.2 mL to 2 mL while the actuator's rotation angle ranges from 90° to 180° under a 10 N·mm payload. The payload torque applied to the actuator is calculated as the product of the weight's gravity and the radius of the cylindrical rod. To enhance repeatability from the outset of data collection, the chamber underwent a break-in process during fabrication, in order for desirable creases to appear. Figure 10a illustrates the relationships between the water volume inside the actuator and the rotation angle of the actuator under different payloads. The data presented in the curves represent the average of three actuator samples. Notably, there is a larger hysteresis observed when the payload is small, attributable to the stiffness of the actuator, which makes folding difficult when the actuator straightens. Moreover, increased payload induces actuator deformation, leading to a decrease in the actuator's rotation angle output due to its inherent flexibility. The folded actuator was driven through 100 full cycles with a 15 N·mm payload. The repeatability test results are shown in Figure 10b, demonstrating the actuator's high repeatability. Figure 10c demonstrates the maximum pressures within the actuator across one actuation cycle at different payloads. The maximum pressure inside the actuator exhibits linearity with the payload when it exceeds 20 N·mm. Additionally, the burst pressure of the actuator was approximately 200 kPa.

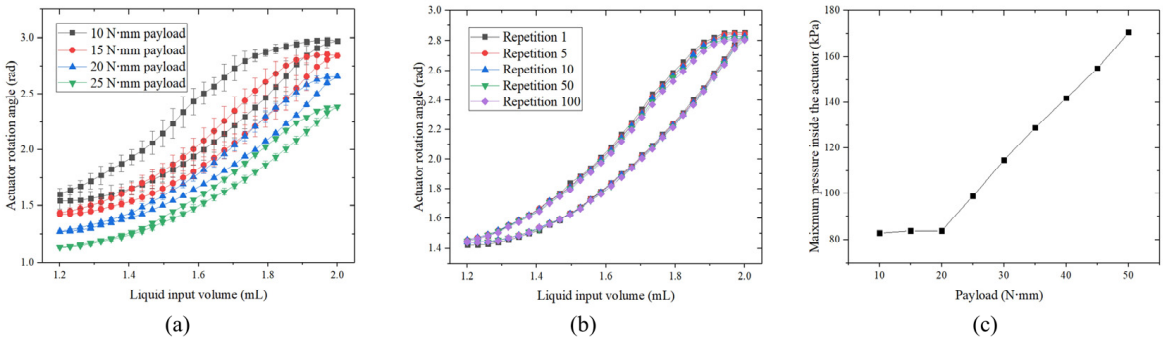

Figure 10. Actuator characteristics. (**a**) The relationships between the water volume injected into the actuator and the actuator's rotation angle under different payload torques. (**b**) The results of 100 cycles of a repeatability test. (**c**) Th maximum pressures inside the actuator across one actuation cycle at different payloads. (All the hysteresis loops are counter-clockwise and all the error bars indicate standard deviation for 3 samples).

The rotation angle of the folded actuator can be determined through the inverse kinematics model. The folded actuator can be controlled by a syringe pump if the relation

between the actuator rotation angle and the water volume inside the actuator is acquired. The mathematical expression used for control is based on the curve-fitting of the experimental data corresponding to the lower black line in Figure 10a, from 1.2 mL to 1.9 mL, with the minimum torque payload. A larger initial torque payload of the actuators would cause larger deformations of the robot's scaffold, which would affect the established kinematics model. The mathematical expression is

$$f(x) = 2.603x^2 - 6.218x + 5.251 \tag{12}$$

where x is the actuator rotation angle and $f(x)$ is the water volume inside the actuator.

Since the cable is made of plastic film, it is essential to test the maximum tension it can withstand. Figure 11a shows the diagram of the cable tensile test setup. A linear stage and an actuator were secured on the bench. The end of the plastic cable was connected to a load cell, which was mounted on the moving platform of the linear stage. The cable was gradually stretched until it reached its breaking point. Figure 11b presents the test results of three separate actuators. The cables could withstand forces exceeding 10 N, resulting in a stretching distance of approximately 20 mm. When the cable tension was below 6 N, the stretching distances remained less than 5 mm for all tested cables.

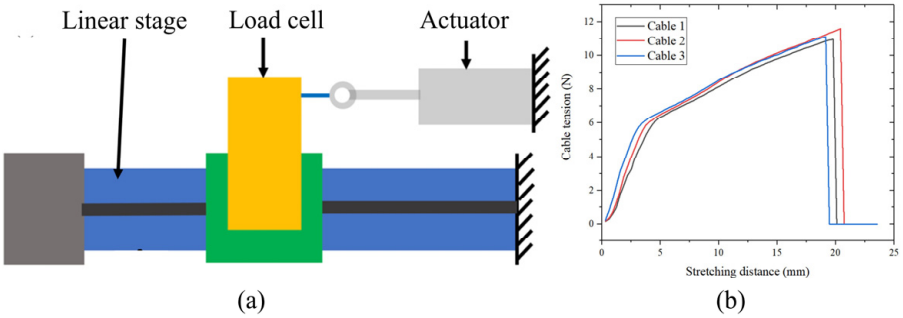

Figure 11. Cable tensile test. (**a**) A platform diagram of the cable tensile test. (**b**) The test results.

3.2. Robot Deployment

The robot, largely constructed from thin plastic films, can be compactly folded before pressurization, making it suitable for natural orifice transluminal surgery applications. As shown in Figure 12a,b, the robot can be folded into a cylinder measuring 110 mm in length and 14 mm in diameter, which satisfies the lower limit of the colon's size for comfortable introduction [27]. Upon inflation, the volume of the scaffold significantly increases, eventually forming a hollow hexagonal prismatic structure with edge lengths of 34 mm and a length of 100 mm (Supplementary Materials). This test and all subsequent experiments are conducted at a scaffold pressure of 100 kPa. Figure 12c,d illustrates the robot's successful deployment within a colon phantom, which has an inner perimeter of 204 mm, equivalent to the perimeter of the deployed scaffold. Within the phantom, the robot assumes the form of a regular hexagonal prism, showcasing its ability to conform to luminal structures effectively. An envisioned operational sequence for the robot involves its deflated state being mounted alongside and enveloped around a carrier endoscope, facilitating delivery through a natural orifice and into the lumen (e.g., the colon). After reaching the designated operative site, the robot stabilizes itself against the lumen wall upon inflating the scaffold, thereby enabling the performance of a surgical procedure. Following the surgical procedure, the robot undergoes deflation, collapse, packing, and extraction from the colon.

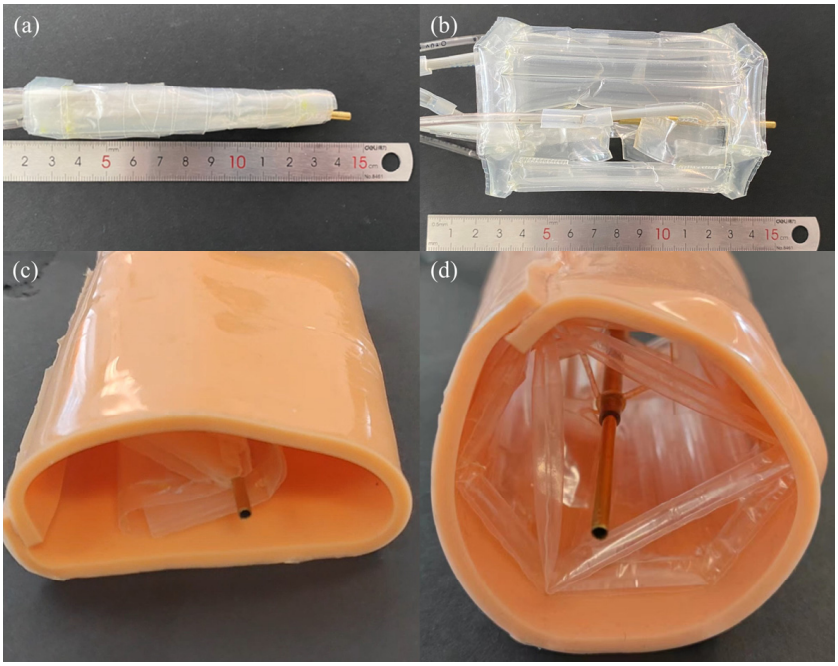

Figure 12. Robot deployment. The robot can deploy from a deflated and folded state to an inflated and undeployed state (**a**,**b**) freely and (**c**,**d**) in a colon phantom.

3.3. Robot Workspace

In MATLAB, the robot is simplified as a CDPR with rigid links, as shown in Figure 13, to simulate its tip workspace. The simulated workspace spans 80 mm, 85 mm, and 36 mm along the X, Y, and Z axes, respectively. Various poses of the robot are illustrated in Figure 14. However, the measured workspace falls short of the theoretical one, measuring 70 mm, 55 mm, and 20 mm along the X, Y, and Z axes, respectively. This discrepancy should be attributed to scaffold flexibility and deformation. Especially at the boundaries of the workspace, the robot approaches its singular configuration, resulting in high tension on some cables. This can lead to significant robot deformation and a decrease in the workspace. Additionally, the triangular support imposes constraints on effector motion, further reducing the workspace. To extend the robot workspace, options include scaling up the entire robot, its repositioning using the host endoscope, or implementing a prismatic joint in the over-tube end-effector.

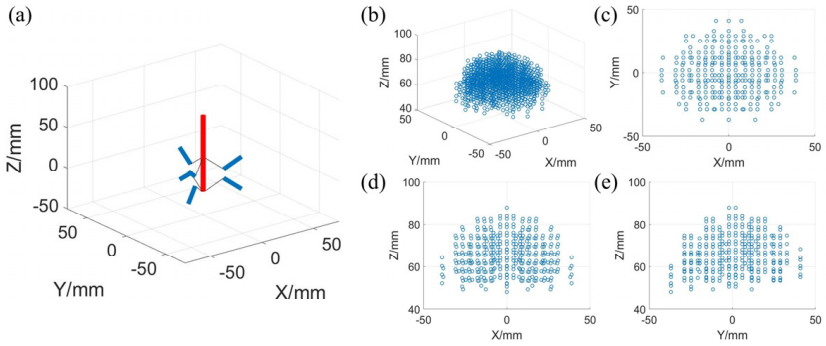

Figure 13. The simulated robot workspace. (**a**) The simplified robot structure in Matlab. The red line indicates the effector, and the blue lines indicate the simplified links. (**b**) The side, (**c**) X-Y plane, (**d**) X-Z plane, and (**e**) Y-Z plane view of the robot workspace.

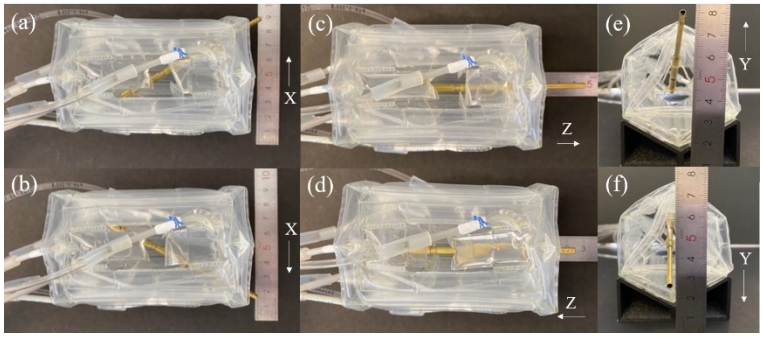

Figure 14. The measured robot workspace. (**a**,**b**) Along the X axis. (**c**,**d**) Along the Z axis. (**e**,**f**) Along the Y axis.

3.4. Scaffold Stiffness Test

The scaffold, crafted from low-stiffness materials with compliance, can achieve rigidity upon inflation, with its stiffness being contingent on pressure. Figure 15a illustrates the setup for testing scaffold stiffness. A rigid plate was affixed to a linear stage, and the inflatable scaffold was secured onto the plate using double-sided tape. Another rigid plate, pressing against a force/torque transducer (Nano 17, ATI Automation, Apex, NC, USA), was adhered to the scaffold. The force/torque transducer, connected to a 16-bit NI USB-6259 DAQ (National Instruments, Austin, TX, USA), was mounted on the moving platform of the linear stage. To pressurize the scaffold, an air pump (OF302-4 B, JUN-AIR, Inc., Racine, WI, USA) was employed, with a pressure regulator (PRE1-U08, AirCom, Ratingen, Germany) adjusting the pressure. Initially, the transducer made contact with the scaffold, marking the starting point where the compression distance is 0 mm. Subsequently, the force transducer compressed the scaffold by 10 mm before retracting to the starting point. This process was repeated four times, with the mean of these repetitions utilized for analysis. Figure 15b shows the correlation between the applied forces and the compression distances at 50 kPa and 100 kPa pressures within the scaffold, respectively. These results illustrate the scaffold's variable stiffness capability. The burst pressure for both the prismatic scaffold and the triangular support is approximately 270 kPa.

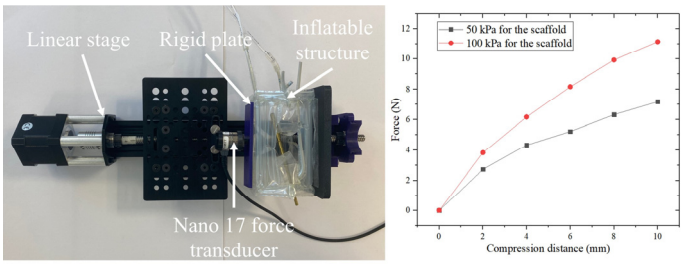

(a) (b)

Figure 15. The scaffold stiffness test. (**a**) The stiffness test's setup. (**b**) The variable stiffness test results.

3.5. Repeatability and Hysteresis Test

During the tracking test, shown in Figure 16a, the OptiTrack optical motion tracking system was utilized to track the position of the robot's tip. Four reflective markers were affixed to the bench to determine the base coordinate system. The robot scaffold was fixed on the bench using double-sided tape. Six syringe pumps were used to drive the actuators. Commands from the laptop were transmitted via a USB to two Arduino Mega2560 boards, with each manipulating three syringe pumps. The open-loop controlled robot tracked a circle with a diameter of 43 mm, repeated ten times (Supplementary Materials). The tracking results are depicted in Figure 16b, while Figure 16c showcases the tracking errors within one cycle. The maximum, mean, and standard deviation for tracking errors amounted to 11.05 mm, 6.00 mm, and 6.65 mm, respectively. The tracking error and the observed

trajectory shape may be attributed to several factors: (1) The deformation of the robot: the inherent flexibility of the inflated beams on the scaffold may deform, causing the actuator to deviate from its intended pose. (2) Unexpected actuator behavior: despite being assumed to have two rigid linkages connected by a 1-DOF revolute joint, the actuator may bend off-plane. The positions of the revolute joints may deviate from their intended positions. (3) The control expression of each actuator is based on a test setup that does not fully reflect the constraints imposed on the actuator by the robot scaffold, which may also introduce slight errors. (4) Manufacturing errors: as seen in Section 2.6, the edge welded manually along the green lines differs from other edges, which introduce slight asymmetries in the scaffold. Nevertheless, the test shows the robot has very high repeatability. The repeatability error was tested by comparing each point to the average value of ten corresponding points in ten cycles. Table 1 shows the maximum, mean, and root mean square errors (RMSEs) for repeatability, indicating that both the mean error and RMSE are smaller than 0.5 mm.

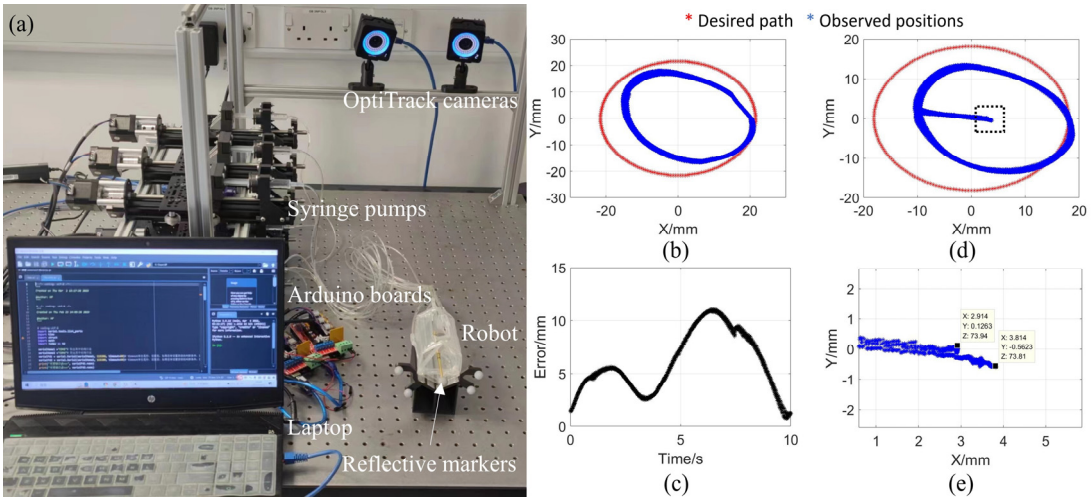

Figure 16. Robot tracking. (**a**) The test setup. (**b**) The results of tracking a 43 mm diameter circle. (**c**) The tracking errors. (**d**) The results of tracking a 36 mm diameter circle. (**e**) An enlarged view around the initial point.

Table 1. The repeatability test results.

	Maximum	Mean	RMSE
Error X/mm	1.1311	0.2661	0.3219
Error Y/mm	0.8929	0.1918	0.2279
Error Z/mm	0.4326	0.0818	0.0993
Absolute error/mm	1.3551	0.3645	0.4186

In theory, the robot should not exhibit hysteresis since the cable is directly connected from the actuator to the effector without any intermediary contact. The hysteresis test procedure involved controlling the tip to execute a circular motion for ten repetitions and then returning to its initial position. The distance between the final and initial positions was used to quantify hysteresis. Only the two rotational DOFs were active during this process, with the rotation center located at the effector axis and the midpoint of the two groups of attachment points. Figure 16d shows this process, and Figure 16e provides an enlarged view around the initial point. Table 2 presents the results of the hysteresis test, where circles of different diameters were tracked. The hysteresis values were all below 2.5 mm. When converted to angle hysteresis, calculated by dividing the position hysteresis by the distance between the robot tip and the rotation center, all four hysteresis angles were below 2°.

Table 2. The hysteresis test results.

Circle Diameter (mm)	29	36	43	50
Position hysteresis (mm)	0.6553	1.065	2.388	2.070
Angle hysteresis (°)	0.5143	0.8359	1.874	1.624

3.6. The Force Exertion of the End-Effector

The end-effector force exertion test platform, shown in Figure 17a, was utilized to evaluate the force exertion capability of the robot, employing a Nano 17 force transducer. A Geomagic Touch haptic device (3D Systems, Littleton, CO, USA), shown in Figure 18a, was used to control the robot, with the pose of the haptic device handle read using Python. The three translation DOFs and the two rotation DOFs of the effector corresponded with those of the haptic device. The motion range of the effector tip was confined within a 30 mm diameter sphere in the simulated workspace after mapping to the effector tip. Forces were recorded as the effector tip moved within the motion range as shown in Figure 17b. The maximum forces measured along each axis are detailed in Table 3. Given the long instrument, the softness of the robot scaffold, and the elasticity of the plastic cables, the force output along the X and Y axes is comparatively lower. According to the measured forces of 0.9 N and 0.58 N for lifting and pulling mucosa in the rectum [29], the force exertion of the end-effector for pulling the mucosa appears to be sufficient. However, the insufficient force for lifting the mucosa may not pose an issue in practice, as, for tissue dissection tasks (such as "peeling off" the mucosa from the submucosa during ESD), retraction in the Z axis holds greater significance. However, this will require validation in subsequent pre-clinical trials.

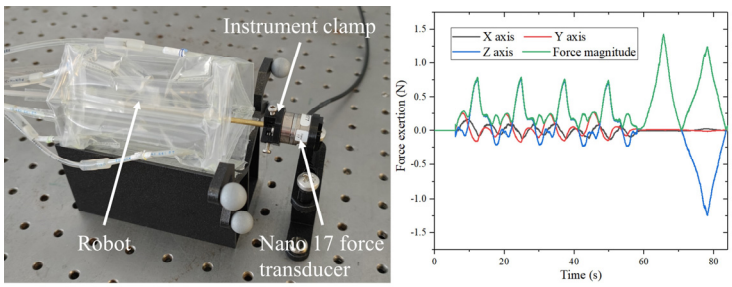

Figure 17. The end-effector's force exertion test. (**a**) The test platform. (**b**) The force exertions by the end-effector in the X, Y, and Z axes and forces' magnitude.

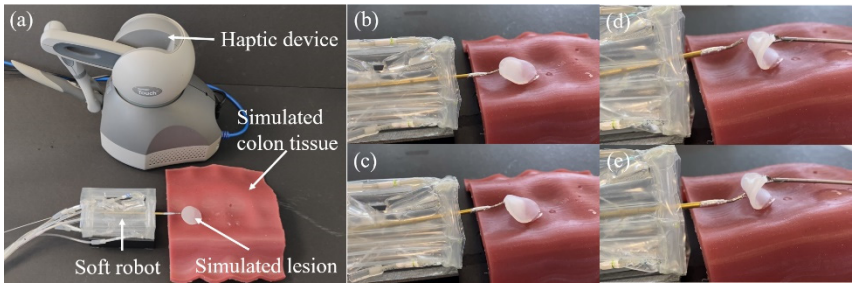

Figure 18. The simulated surgical experiments. (**a**) The experimental platform. (**b**,**c**) The lifting of a simulated tissue. (**d**,**e**) The performing of a 'Sweep' motion.

Table 3. The maximum forces measured in each axis.

Direction	+X	-X	+Y	-Y	+Z	-Z
Force/N	0.17	0.13	0.27	0.17	1.43	1.25

3.7. Simulated Surgical Tasks

The setup for conducting simulated surgical operations, such as lifting and dissecting cancerous tissues, as shown in Figure 18, which are fundamental steps in ESD, involved integrating a grasper into the effector over-tube. A circular silicone piece, approximately 27 mm in diameter, was affixed onto the silicone colon phantom to simulate a cancerous tissue on the colon. As shown in Figure 18b,c, the grasper was manipulated to approach and grasp the simulated lesion, subsequently lifting the simulated tissue. Additionally, Figure 18d,e demonstrates the robot's capability to execute a 'sweep' motion, with the over-tube moving leftward and rightward to simulate the diathermy dissecting the lesion (Supplementary Materials). These basic simulated surgical operations were conducted to showcase the potential applicability of the robot in MISs. Furthermore, the robot's durability was evaluated through hours of testing without observed breakage, indicating its sufficient durability as a single-use surgical device.

4. Discussion and Conclusions

A novel, soft, CDPR for MISs based on folded pouch actuators is introduced, featuring variable stiffness capabilities. The rapid and cost-effective production of this type of robot allows for single-use applications. The direct connection of the end-effector to the actuators eliminates the friction typically associated with Bowden tubes, mitigating potential hysteresis issues.

Several planar robots have been prototyped based on folded hydraulic actuators, which are low profile, low cost, and have a large stroke. The actuator has a simple structure and can work as a robotic arm, opening avenues for the creation of innovative mechanisms and structures. Deployable robots with diverse configurations could be crafted using the same manufacturing technique. For instance, redundant CDPRs could be produced to enhance the robot's force capabilities and workspace. CDPRs with more compact configurations can be explored to reduce the longitudinal size for easier delivery in lumens and to improve the scaffold stiffness.

This paper focuses on designing a novel CDPR, including its actuators and deployable scaffold. Future work will explore appropriate approaches for the full deflation, folding, and extraction of the robot from the colon. The robot allows for the intuitive execution of surgical tasks through small manual adjustments by the user in master-slave mode. Its accuracy can be further improved using closed-loop control methods, such as data-driven techniques or visual serving. However, establishing a kinematic model that considers robot deformation would further improve the accuracy and prediction of the robot workspace, and allow for the estimation of the robot's force output. Electrical Impedance Tomography (EIT) techniques developed in [31] will be used for actuator and/or scaffold shape sensing for the above purposes. Sensors, such as pressure sensors, will be integrated to monitor system operation to prevent complications from potential robot failures. Subsequently, the robot will be integrated into an endoscopic system to verify its feasibility in in vivo scenarios.

Supplementary Materials: The following supporting information can be downloaded at: https://www.mdpi.com/article/10.3390/app14104095/s1, Video S1: Demonstrations of the robots.

Author Contributions: Conceptualization, J.Y.; Methodology, J.Y., M.R. and J.A.; Investigation, J.Y., X.L., M.R. and Z.Z.; Writing—original draft, J.Y. and X.L.; Writing—review & editing, J.A., Z.Z., Z.S. and G.M.; Supervision, Z.S. and G.M.; Project administration, G.M. All authors have read and agreed to the published version of the manuscript.

Funding: This research was funded in part by the National Natural Science Foundation of China (No. 52275058) and the Fundamental Research Funds for the Central Universities (No. NJ2022007). James Avery is an Imperial College Research Fellow.

Institutional Review Board Statement: Not applicable.

Informed Consent Statement: Not applicable.

Data Availability Statement: The data presented in this study is available on request from the corresponding author. The data is not publicly available because the dataset was jointly completed by the team.

Conflicts of Interest: The authors declare no conflict of interest.

References

1. Yeung, B.P.M.; Chiu, P.W.Y. Application of robotics in gastrointestinal endoscopy: A review. *World J. Gastroenterol.* **2016**, *22*, 1811. [CrossRef]
2. Tada, N.; Sumiyama, K. Robotic Platforms for Therapeutic Flexible Endoscopy: A Literature Review. *Diagnostics* **2024**, *14*, 595. [CrossRef] [PubMed]
3. Gifari, M.W.; Naghibi, H.; Stramigioli, S.; Abayazid, M. A review on recent advances in soft surgical robots for endoscopic applications. *Int. J. Med. Robot. Comput. Assist. Surg.* **2019**, *15*, e2010. [CrossRef]
4. Runciman, M.; Darzi, A.; Mylonas, G.P. Soft robotics in minimally invasive surgery. *Soft Robot.* **2019**, *6*, 423–443. [CrossRef]
5. Zhang, D. *Parallel Robotic Machine Tools*; Springer Science & Business Media: Berlin/Heidelberg, Germany, 2009.
6. Khalifa, A.; Fanni, M.; Mohamed, A.M.; Miyashita, T. Development of a new 3-DOF parallel manipulator for minimally invasive surgery. *Int. J. Med. Robot. Comput. Assist. Surg.* **2018**, *14*, e1901. [CrossRef] [PubMed]
7. Liu, Q.; Zhang, X.; Wang, C.; Zhang, B.; Shang, W.; Lin, Z.; Duan, L.; Wu, Z.; Fujie, M.G. System Design of A Dual-Arm Surgical Robot for Single Port Access Surgery. In Proceedings of the 2018 IEEE International Conference on Intelligence and Safety for Robotics (ISR), Shenyang, China, 24–27 August 2018; IEEE: Piscataway, NJ, USA, 2018; pp. 349–354.
8. Li, C.; Gu, X.; Xiao, X.; Lim, C.M.; Ren, H. A robotic system with multichannel flexible parallel manipulators for single port access surgery. *IEEE Trans. Ind. Inform.* **2018**, *15*, 1678–1687. [CrossRef]
9. Orekhov, A.L.; Black, C.B.; Till, J.; Chung, S.; Rucker, D.C. Analysis and validation of a teleoperated surgical parallel continuum manipulator. *IEEE Robot. Autom. Lett.* **2016**, *1*, 828–835. [CrossRef]
10. Pott, A. *Cable-Driven Parallel Robots*; Bruckmann, T., Ed.; Springer: Berlin/Heidelberg, Germany, 2013; pp. 119–134.
11. Mylonas, G.P.; Vitiello, V.; Cundy, T.P.; Darzi, A.; Yang, G.Z. CYCLOPS: A versatile robotic tool for bimanual single-access and natural-orifice endoscopic surgery. In Proceedings of the 2014 IEEE International Conference on Robotics and Automation (ICRA), Hong Kong, China, 31 May–7 June 2014; IEEE: Piscataway, NJ, USA, 2014; pp. 2436–2442.
12. Runciman, M.; Avery, J.; Zhao, M.; Darzi, A.; Mylonas, G.P. Deployable, variable stiffness, cable driven robot for minimally invasive surgery. *Front. Robot. AI* **2020**, *6*, 141. [CrossRef] [PubMed]
13. Runciman, M.; Avery, J.; Darzi, A.; Mylonas, G. Open Loop Position Control of Soft Hydraulic Actuators for Minimally Invasive Surgery. *Appl. Sci.* **2021**, *11*, 7391. [CrossRef]
14. Niiyama, R.; Rus, D.; Kim, S. Pouch motors: Printable/inflatable soft actuators for robotics. In Proceedings of the 2014 IEEE International Conference on Robotics and Automation (ICRA), Hong Kong, China, 31 May–7 June 2014; IEEE: Piscataway, NJ, USA, 2014; pp. 6332–6337.
15. Kwon, J.; Yoon, S.J.; Park, Y.L. Flat inflatable artificial muscles with large stroke and adjustable force–length relations. *IEEE Trans. Robot.* **2020**, *36*, 743–756. [CrossRef]
16. Xie, D.; Liu, J.; Zuo, S. Pneumatic artificial muscle with large stroke based on a contraction ratio amplification mechanism and self-contained sensing. *IEEE Robot. Autom. Lett.* **2021**, *6*, 8599–8606. [CrossRef]
17. Oh, N.; Park, Y.J.; Lee, S.; Lee, H.; Rodrigue, H. Design of paired pouch motors for robotic applications. *Adv. Mater. Technol.* **2019**, *4*, 1800414. [CrossRef]
18. Jang, J.H.; Jamil, B.; Moon, Y.; Coutinho, A.; Park, G.; Rodrigue, H. Design of Gusseted Pouch Motors for Improved Soft Pneumatic Actuation. In *IEEE/ASME Transactions on Mechatronics*; IEEE: Piscataway, NJ, USA, 2023.
19. Yang, H.D.; Greczek, B.T.; Asbeck, A.T. Modeling and analysis of a high-displacement pneumatic artificial muscle with integrated sensing. *Front. Robot. AI* **2019**, *5*, 136. [CrossRef] [PubMed]
20. Yang, H.D.; Cooper, M.; Akbas, T.; Schumm, L.; Orzel, D.; Walsh, C.J. A soft inflatable wearable robot for hip abductor assistance: Design and preliminary assessment. In Proceedings of the 2020 8th IEEE RAS/EMBS International Conference for Biomedical Robotics and Biomechatronics (BioRob), New York, NY, USA, 29 November–1 December 2020; IEEE: Piscataway, NJ, USA, 2020; pp. 692–699.
21. Chung, J.; Heimgartner, R.; O'Neill, C.T.; Phipps, N.S.; Walsh, C.J. Exoboot, a soft inflatable robotic boot to assist ankle during walking: Design, characterization and preliminary tests. In Proceedings of the 2018 7th IEEE International Conference on Biomedical Robotics and Biomechatronics (biorob), Enschede, The Netherlands, 26–29 August 2018; IEEE: Piscataway, NJ, USA, 2018; pp. 509–516.
22. O'Neill, C.T.; McCann, C.M.; Hohimer, C.J.; Bertoldi, K.; Walsh, C.J. Unfolding textile-based pneumatic actuators for wearable applications. *Soft Robot.* **2022**, *9*, 163–172. [CrossRef] [PubMed]
23. Ge, L.; Chen, F.; Wang, D.; Zhang, Y.; Han, D.; Wang, T.; Gu, G. Design, modeling, and evaluation of fabric-based pneumatic actuators for soft wearable assistive gloves. *Soft Robot.* **2020**, *7*, 583–596. [CrossRef] [PubMed]
24. Chung, S.; Coutinho, A.; Rodrigue, H. Manufacturing and Design of Inflatable Kirigami Actuators. *IEEE Robot. Autom. Lett.* **2022**, *8*, 25–32. [CrossRef]

25. Yang, D.; Feng, M.; Gu, G. High-stroke, High-Output-Force, Fabric-Lattice Artificial Muscles for Soft Robots. *Adv. Mater.* **2023**, *36*, 2306928. [CrossRef]
26. Feng, M.; Yang, D.; Ren, L.; Wei, G.; Gu, G. X-crossing pneumatic artificial muscles. *Sci. Adv.* **2023**, *9*, eadi7133. [CrossRef] [PubMed]
27. Alazmani, A.; Hood, A.; Jayne, D.; Neville, A.; Culmer, P. Quantitative assessment of colorectal morphology: Implications for robotic colonoscopy. *Med. Eng. Phys.* **2016**, *38*, 148–154. [CrossRef]
28. Repici, A.; Hassan, C.D.P.P.D.; Pessoa, D.D.P.; Pagano, N.; Arezzo, A.; Zullo, A.; Lorenzetti, R.; Marmo, R. Efficacy and safety of endoscopic submucosal dissection for colorectal neoplasia: A systematic review. *Endoscopy* **2012**, *44*, 137–150. [CrossRef] [PubMed]
29. Ranzani, T.; Ciuti, G.; Tortora, G.; Arezzo, A.; Arolfo, S.; Morino, M.; Menciassi, A. A novel device for measuring forces in endoluminal procedures. *Int. J. Adv. Robot. Syst.* **2015**, *12*, 116. [CrossRef]
30. Gouttefarde, M.; Merlet, J.P.; Daney, D. Wrench-feasible workspace of parallel cable-driven mechanisms. In Proceedings of the 2007 IEEE International Conference on Robotics and Automation, Roma, Italy, 10–14 April 2007; IEEE: Piscataway, NJ, USA, 2007.
31. Avery, J.; Runciman, M.; Darzi, A.; Mylonas, G.P. Shape sensing of variable stiffness soft robots using electrical impedance tomography. In Proceedings of the 2019 International Conference on Robotics and Automation (ICRA), Montreal, QC, Canada, 20–24 May 2019; pp. 9066–9072.